Research Article Vol. 6, No. 12 / December 2019 / Optica 1498

Microwave-to-optical conversion using lithium niobate thin-film acoustic resonators

Linbo Shao,[1,6] Mengjie Yu,[1] Smarak Maity,[1] Neil Sinclair,[1,2] Lu Zheng,[3] Cleaven Chia,[1] Amirhassan Shams-Ansari,[1] Cheng Wang,[1,4] Mian Zhang,[1,5] Keji Lai,[3] and Marko Lončar[1,7]

[1]John A. Paulson School of Engineering and Applied Sciences, Harvard University, 29 Oxford Street, Cambridge, Massachusetts 02138, USA
[2]Division of Physics, Mathematics and Astronomy, and Alliance for Quantum Technologies (AQT), California Institute of Technology, 1200 E. California Blvd., Pasadena, California 91125, USA
[3]Department of Physics, University of Texas at Austin, Austin, Texas 78712, USA
[4]Department of Electrical Engineering & State Key Laboratory of THz and Millimeter Waves, City University of Hong Kong, Kowloon, Hong Kong, China
[5]HyperLight Corporation, 501 Massachusetts Avenue, Cambridge, Massachusetts 02139, USA
[6]e-mail: shaolb@seas.harvard.edu
[7]e-mail: loncar@seas.harvard.edu

Received 8 July 2019; revised 9 September 2019; accepted 10 September 2019 (Doc. ID 372069); published 2 December 2019

Acoustic or mechanical resonators have emerged as a promising means to mediate efficient microwave-to-optical conversion. Here, we demonstrate conversion of microwaves up to 4.5 GHz in frequency to 1500 nm wavelength light using optomechanical interactions on suspended thin-film lithium niobate. Our method uses an interdigital transducer that drives a freestanding 100 μm-long thin-film acoustic resonator to modulate light traveling in a Mach–Zehnder interferometer or racetrack cavity. The strong microwave-to-acoustic coupling offered by the transducer in conjunction with the strong photoelastic, piezoelectric, and electro-optic effects of lithium niobate allows us to achieve a half-wave voltage of $V_\pi = 4.6$ V and $V_\pi = 0.77$ V for the Mach–Zehnder interferometer and racetrack resonator, respectively. The acousto-optic racetrack cavity exhibits an optomechanical single-photon coupling strength of 1.1 kHz. To highlight the versatility of our system, we also demonstrate a microwave photonic link with unitary gain, which refers to a 0 dB microwave power transmission over an optical channel. Our integrated nanophotonic platform, which leverages the compelling properties of lithium niobate, could help enable efficient conversion between microwave and optical fields.

https://doi.org/10.1364/OPTICA.6.001498

1. INTRODUCTION

Conversion of information between the microwave and optical domains is a key ingredient for classical and quantum hybrid signal processing, computing, and networking [1–5]. Among the many approaches to achieve coherent quantum transduction, electrically coupled optomechanical systems have emerged as promising candidates [6]. Experimental progress includes suspended structures such as optical waveguides in microwave cavities [7], membranes in free-space Fabry–Perot cavities [8–10], and nanoscale piezoelectric optomechanical crystals (OMCs) [11–16]. While optical waveguides in bulk microwave cavities benefit from the high quality (Q) factors of microwave resonance, the suspended membranes achieve a high photon number conversion efficiency leveraging a triple resonance of microwave, mechanical, and optical fields. Large-scale integration of these devices is, however, challenging and has not been demonstrated yet. On the other hand, OMCs [17–22] provide a fully integrated platform featuring gigahertz mechanical frequencies, and megahertz optomechanical coupling strengths, while limitations due to surface effects are becoming better understood [17]. Microwave-to-mechanical (i.e., electromechanical) coupling to OMCs has been achieved using piezoelectric materials, such as aluminum nitride [14–16], gallium arsenide [11,13], and lithium niobate (LN) [12]. However, the demonstrated electromechanical couplings are inefficient due to the mismatch between the mechanical resonant modes to microwaves [12,15,16] or traveling mechanical waves [11,13,14].

To address the weak microwave-to-mechanical conversion of current integrated devices, we use freestanding LN thin-film acoustic (i.e., mechanical) resonators with low-loss optical resonators. Using an interdigital transducer (IDT), our acousto-optic devices demonstrate up to 50% coupling efficiency from microwave inputs to acoustic resonator modes, thereby enabling efficient optical modulation using Mach–Zehnder interferometers (MZIs) and racetrack cavities. Our approach benefits from the strong piezoelectricity and electro-optic effects of LN [23–25] in conjunction with the photoelastic effect to achieve microwave-to-optical conversion. Specifically, using a 100 μm-long optical waveguide embedded within a 3.33 GHz acoustic resonator with a Q factor of 3600, our MZI exhibits a low

half-wave voltage V_π of 4.6 V. Moreover, the half-wave-voltage-length product $V_\pi L$, the figure of merit for optical modulators, is as low as 0.046 V · cm, which is a 50-fold reduction over state-of-the-art electro-optic modulators [26]. This low $V_\pi L$ comes at the expense of reduced microwave-to-optical conversion bandwidth of around 1 MHz, which is significantly smaller than that of electro-optic MZI approaches [26]. Nonetheless, it is much greater than what has previously been demonstrated using a microwave, mechanical, and optical triple resonance [8]. Our racetrack cavity features an optical Q factor of over 2×10^6, thereby enabling single optical sideband conversion with an effective V_π of 0.77 V, a photon number conversion efficiency of 0.0017% for an optical power of 1 mW, and an acousto-optic (i.e., optomechanical) coupling strength of 1.1 kHz. Though this acousto-optic coupling strength is lower than that of state-of-the-art OMCs, the overall microwave-to-optical conversion efficiency is improved due to the enhanced microwave-to-mechanical coupling. Finally, to illustrate its efficient microwave-to-optical conversion, we demonstrate a loss-less microwave-photonic link with a ∼50 mW optical power routing on chip.

2. DEVICE DESIGN AND FABRICATION

IDTs are periodically spaced metal electrodes placed on piezoelectric materials and provide efficient transduction between alternating electric fields and acoustic waves when the electrode spacing matches the wavelength of the acoustic wave. We utilize IDTs to drive our acoustic resonators due to their efficient electromechanical coupling and ease of fabrication. Notably, IDTs are widely used in electro-acoustic signal processing at up to hypersonic (greater than 1 GHz) frequencies [27]. Furthermore, they have been used in optical applications to diffract guided beams [28–30], modulate cavities [31], drive photonic molecules [32], and even break time-reversal symmetry [33]. Therefore, integration of IDT-coupled acoustic resonators [34,35] with high-performance optical devices fabricated in LN [36,37] offers the possibility for efficient acoustically mediated microwave-to-optical conversion.

Figures 1(a) and 1(b) shows our acousto-optic devices in the MZI and the racetrack cavity configurations, respectively. IDT-coupled acoustic resonators host optical waveguides and modulate the phase acquired by the optical signal propagating in one arm of the MZI, which results in intensity modulation of the transmitted optical signal [Fig. 1(a)]. A similar effect is responsible for modulating the optical resonance of the racetrack cavity [Fig. 1(b)]. For our optical components, we employ rib waveguides that are defined by etching a 0.8-μm-thick X-cut LN thin film to a depth of 0.4 μm. The width of the optical waveguide is 0.95 and 1.3 μm in the case of MZI and the racetrack cavity, respectively. In the case of the latter, the larger waveguide cross section is used to reduce the propagating loss due to sidewall roughness. To reduce bending loss and to minimize mode conversion between transverse electric (TE) and transverse magnetic (TM) modes, we employ quadratic Bézier curves for our optical waveguides, which is a generalized form of more conventional Euler curves [38]. To confine the acoustic waves, the LN waveguide is released by removing a sacrificial silicon dioxide layer [Fig. 1(c)]. The suspended thin-film acoustic resonator is formed by the long slots on both sides of an LN waveguide section. The length of each acoustic resonator is 10 μm, and the width is 100 μm. The electrode width of 90 μm is used to match the impedance of IDT with the 50 Ω impedance of the driving electronics. The electrode pitch and width of IDTs are controlled to allow excitation of acoustic modes at different frequencies. Specifically, an IDT with four electrodes, a pitch of 0.6 μm, and a width of 0.3 μm is used for the acoustic resonator in the MZI configuration. This allows the coupling to acoustic modes in the range of 1–4.5 GHz, with peak coupling efficiency occurring around 3 GHz. In the racetrack cavity configuration, we use an IDT featuring a pitch of 0.86 μm, a width of 0.43 μm, and the same number of electrodes (four). This allows the highest coupling efficiency to acoustic modes around 2 GHz.

To fabricate each device, three layers of electron beam lithography are used to define the LN optical waveguides, the opening slots for the acoustic resonator and the release of the LN layer, and the metal electrodes needed for IDT. The LN is etched using reactive ion etching, and the fabricated devices feature a sidewall angle of 70°. The metal electrodes are defined using a lift-off process: PMMA resist is patterned as a sacrificial layer, then a

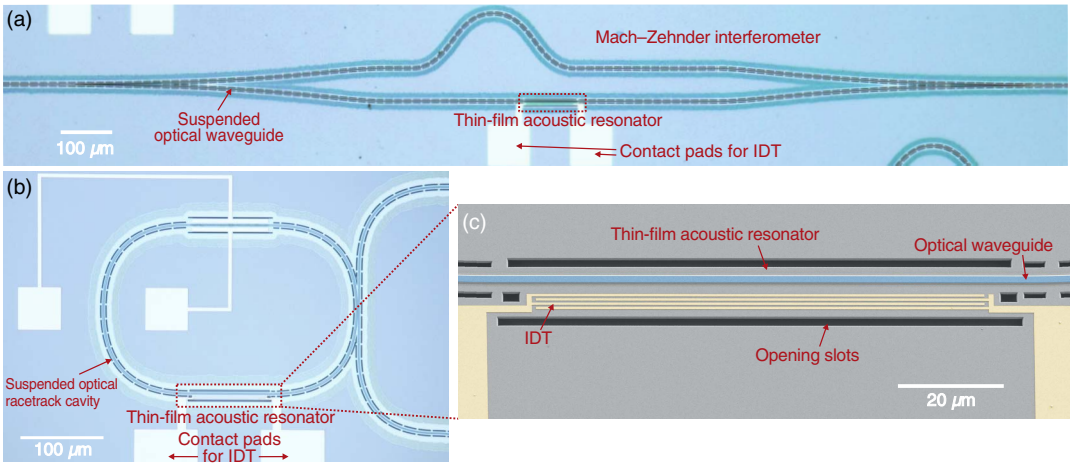

Fig. 1. Integrated acousto-optic devices on suspended thin-film LN. (a) Microscope image of a suspended acousto-optic MZI. The interferometer is unbalanced to allow phase control by laser detuning. (b) Microscope image of a suspended optical racetrack cavity with a thin-film acoustic resonator. The suspended regions adjacent to the optical waveguide are identified by a different color, which is darker than the plain substrate in (a) and lighter in (b). (c) False-color scanning electron microscope image of the acoustic resonator with an IDT and an optical waveguide.

75-nm-thick gold layer with an 8-nm-thick chromium adhesion layer is deposited using electron-beam evaporation, and the device is immersed in a solvent to lift off the resist. Finally, the release of the LN device from the substrate is achieved using buffered oxide etchant, which removes the sacrificial oxide layer underneath through the completely etched slots of the LN layer.

3. DESCRIPTION OF ACOUSTICALLY MEDIATED MICROWAVE-TO-OPTICAL CONVERSION

Our acoustic resonator mediates the microwave-to-optical conversion by coupling to the microwave input via the IDT and modulating light due to acoustic modes [Fig. 2(a)]. The optical modulation is enabled by a generalized acousto-optic interaction that comprises conventional optomechanical couplings of photoelastic and weak moving boundary effects, as well as cascading piezoelectric and electro-optic effects, which feature a coupling strength comparable to photoelastic alone. We perform simulations to understand and engineer the interplay among these three effects in order to maximize the overall acousto-optic interaction.

The coupling strength of each interaction is evaluated using a two-dimensional (2D) numerical model based on the device cross section and crystal orientation shown in Fig. 2(b). To avoid double-counting the coupling strength, we use photoelastic (electro-optic) coefficients under a constant electric field (strain, i.e., clamped) condition following that presented in Refs. [25,39]. Owing to the LN crystal orientation chosen for our device, the generalized acousto-optic interaction is much stronger for the guided TE mode [Fig. 2(c)] than for the TM mode at 1550 nm, due to the strong electro-optic and photoelastic coefficients, r_{33} and p_{31}, respectively, for TE polarization. The electro-optic coefficients form a third-order tensor, and r_{33} relates n_{ZZ}, the optical index change of the crystal ZZ component (indicated by the first 3 in the subscript), to $\mathcal{E}_Z$, the electrical field in the Z direction (indicated by the first 3 in the subscript). The photoelastic coefficients form a fourth-order tensor, and p_{31} relates n_{ZZ} to s_{XX}, the strain of the crystal XX component (indicated by the 1 in the subscript). Thus, the strain s_{XX} (or s_{yy} in the simulation coordinate) contributes most to the photoelastic interaction. Detailed discussions are provided in Supplement 1. Figures 2(d) and 2(e) plot the simulated acoustic strain s_{yy} and electric field $\mathcal{E}_x$ of a 3.24 GHz mode, both of which have the same sign across the optical waveguide region, thus contributing constructively to the overall modulation to the optical refractive index.

The contributions of moving boundary, electro-optic, and photoelastic effects are calculated by integrating the products of the acoustic and optical field components with the corresponding coupling matrices. Acousto-optic interaction strengths between various acoustic modes and optical TE or TM mode are summarized in Table S1 of Supplement 1. For the 3.24 GHz acoustic mode, Figs. 2(f) and 2(g) show the induced refractive index changes of the TE mode by the photoelastic and electro-optic effects. Based on this result, we extract an acousto-optic single-photon coupling strength $g_0 = 1.6$ kHz for the racetrack cavity geometry. For the acousto-optic MZI, the half-wave voltage-length product $V_\pi L$ depends on the acoustic Q factor and microwave-to-acoustic coupling efficiency, where we use experimental values to avoid overestimation by the 2D simulation. A half-wave voltage-length product $V_\pi L = 0.045$ V · cm for the acousto-optic MZI is extracted based on the simulated interaction strength, as well as the acoustic Q of 2000 and electrical-to-acoustic coupling efficiency of 0.5 (corresponding to a -3 dB dip in the S_{11} spectrum) from typical experimental measurements. Details are provided in Section 1 of Supplement 1.

4. ACOUSTO-OPTIC MZI

We experimentally characterize our acousto-optic MZI using a tunable C-band laser, a vector network analyzer (VNA), and a photoreceiver that features a sensitivity of ~800 V/W [Fig. 3(a)].

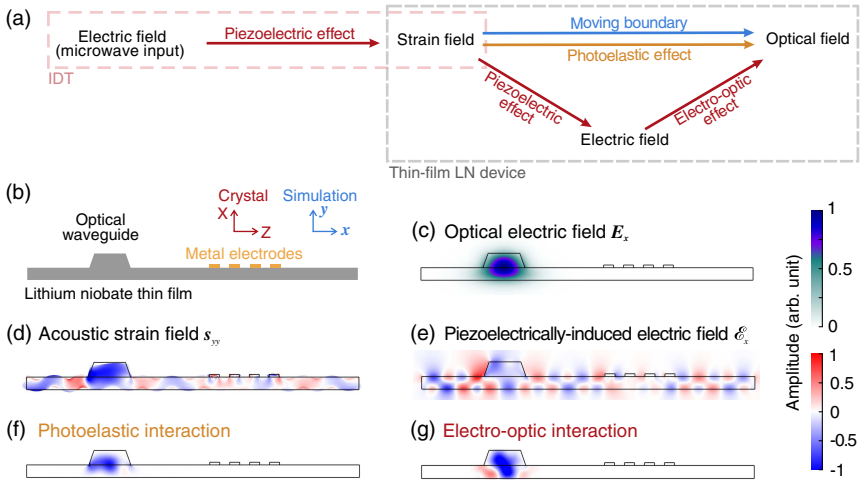

Fig. 2. Numerical simulation of the acoustically mediated microwave-to-optical conversion. (a) Couplings between the microwave, acoustic, and optical fields that facilitate a microwave-to-optical conversion; (b) device schematic used for the 2D numerical simulation. The crystal orientation and coordinate system are shown. The top width of the optical waveguide is 0.95 μm. (c) Electric field E_x of the fundamental TE optical mode; (d) s_{yy} component of the acoustic strain field for the 3.24 GHz acoustic mode, and resulting (e) electric fields $\mathcal{E}_x$ induced by the piezoelectric effect. We note that s_{yy} has the largest contribution to the photoelastic interaction shown in (f). (g) Electro-optic interactions between the optical TE mode and acoustic fields, mediated by the piezoelectric effect. In (f) and (g), the interaction is described by an induced optical refractive index change, calculated by multiplying the optical electric field, the acoustic field, and the interaction matrices. Color scale bars in (d) and (e) are normalized individually, while those in (f) and (g) are the same.

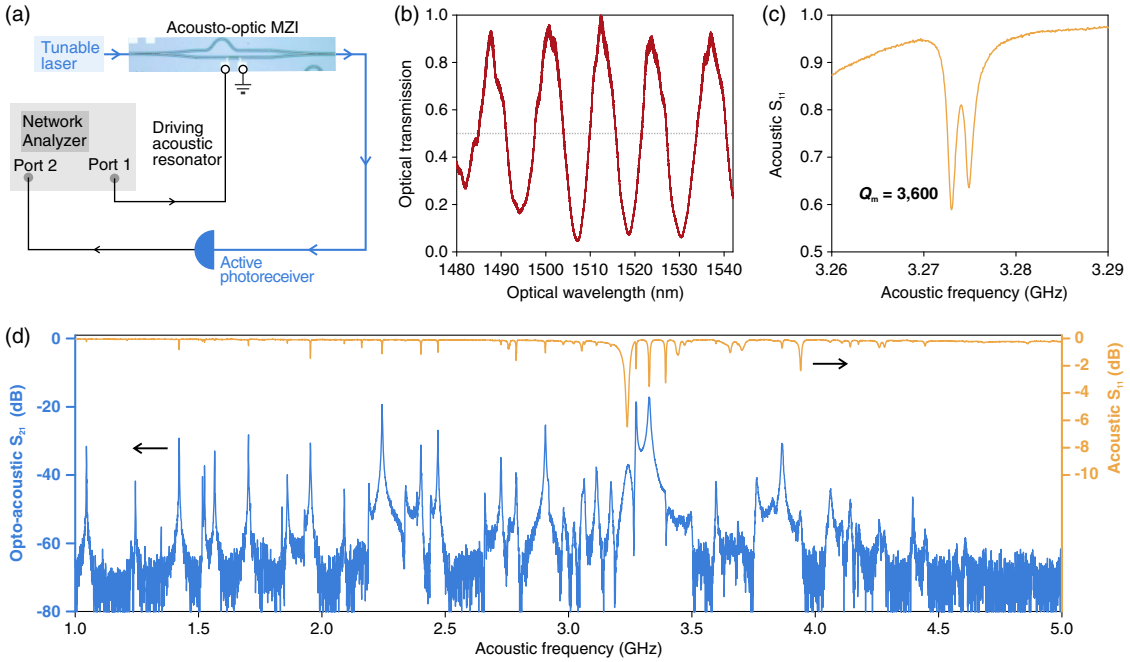

Fig. 3. Characterization of the acousto-optic MZI. (a) Simplified experimental schematic; (b) optical transmission of the acousto-optic MZI; (c) S_{11} reflection spectrum of the acoustic resonator; (d) S_{21} spectrum showing an enhanced microwave-to-optical conversion at the resonances indicated by the S_{11} spectrum. The optical power detected by the photoreceiver is 0.25 mW.

We use lensed fiber to couple light into and out of our structures with a fiber-to-fiber insertion loss of 10 dB (< 5 dB/facet) for our suspended LN chip. The periodic variation of optical transmission with wavelength at 10 nm intervals is consistent with the optical path difference in the MZI [Fig. 3(b)]. To optimize the microwave-to-optical conversion efficiency, the laser wavelength is chosen to be 1534 nm, corresponding to 50% transmission and indicating a $\pi/2$ phase difference between two optical paths.

We evaluate the acoustic resonances and the microwave-to-acoustic coupling of our devices by measuring the microwave reflection (S_{11}) of the IDT. Our acoustic resonator exhibits multiple resonances in the range between 1.0 and 4.5 GHz. To correlate measured acoustic modes with that of our simulations, the acoustic-electric field profiles are experimentally measured using transmission-mode microwave impedance microscopy [40,41]; see Section 4 of Supplement 1. We measure acoustic Q factors of up to 3600 [Fig. 3(c)], similar to the LN OMC devices [12,18], and our resonance at the microwave frequency of 3.273 GHz yields a state-of-the-art frequency-quality-factor product of $fQ > 10^{13}$ at room temperature [35].

We characterize the optical modulation induced by the acoustic resonance by the optoacoustic S_{21} spectrum, where the driving Port 1 of the VNA is connected to the IDT of the acoustic resonator and the detecting Port 2 is connected to the photoreceiver [Fig. 3(a)]. The S_{21} spectrum shown in Fig. 3(d) features several peaks indicating enhanced microwave-to-optical conversion at acoustic resonances, with the strongest responses measured at the 2.24 and 3.33 GHz acoustic modes, in agreement with our simulations (Table S1). The microwave-to-optical conversion efficiency indicated by the S_{21} depends on both the acoustic Q factor and the overlap between the acoustic mode and the optical mode. We extract the half-wave voltage V_π of our acousto-optic MZI from the experimental measurements of the S_{21} spectrum. Under the conditions of our measurement, the MZI half-wave voltage V_π is related to the S_{21} by

$$S_{21} = \left(\frac{\pi R_{\mathrm{PD}} I_{\mathrm{rec}}}{V_\pi}\right)^2, \tag{1}$$

in which R_{PD} ($I_{\mathrm{rec}} = 0.25$ mW) is the sensitivity of (optical power at) the photoreceiver, with derivation given in Section 2 of Supplement 1. We find $V_\pi = 4.6$ V (5.8 V) using $S_{21} = -17.4$ dB (-19.3 dB) at the resonance frequency of 3.33 GHz (2.24 GHz), and due to the 100-μm length of our acoustic resonator, we obtain $V_\pi L = 0.046$ V · cm (0.058 V · cm), which agrees with that predicted by our simulation.

5. ACOUSTO-OPTIC RACETRACK CAVITY

We can further improve the microwave-to-optical conversion efficiency by using the acoustic-optic racetrack cavity [Fig. 4(a)]. Compared with MZI, our racetrack cavity features a loaded optical Q factor of 2.2×10^6 for TE-polarized light of wavelength 1574.9 nm, corresponding to a linewidth of 95 MHz [Fig. 4(b)], allowing us to operate in the microwave sideband-resolved regime. With the laser blue-detuned by the acoustic resonant frequency from the optical resonance, we generate an optical sideband by the acoustic resonant mode and enhance it using the racetrack resonator [Fig. 4(a)]. Consequently, we observe a high $S_{21} = -7.5$ dB at the acoustic resonant frequency of 2 GHz, with a total optical power of $I_{\mathrm{rec}} = 0.13$ mW measured at the photoreceiver [Fig. 4(c)]. We note that the S_{21} quadratically depends on the optical power, and we should consider S_{21} at the same optical power level to compare the conversion efficiency. The S_{21} of the racetrack cavity thus results in a much lower effective V_π of 0.77 V than does the MZI, as determined by

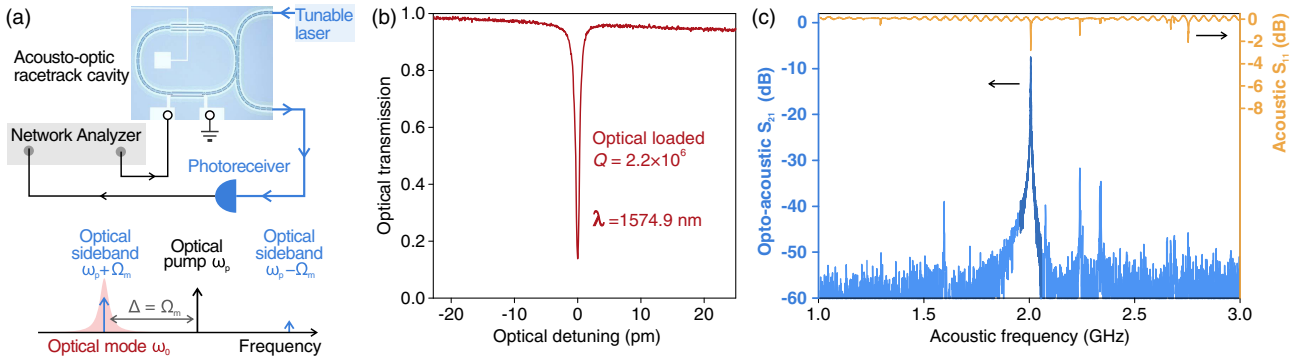

Fig. 4. Characterization of the acousto-optic racetrack cavity. (a) Simplified experimental schematic and illustration of single-sideband microwave-to-optical conversion using an acousto-optic cavity; (b) transmission spectrum of a high-Q optical resonance; (c) acoustic S_{11} and opto-acoustic S_{21} spectra. A high resolution measurement around 2 GHz is shown in dark blue. The optical pump wavelength is set to maximize the power received at the photoreceiver.

the small-signal response of an intensity modulator (see Section 2 of Supplement 1).

Next, we determine the overall acousto-optic single-photon coupling strength g_0. In the sideband-resolved regime ($\Omega_m \gg \kappa$) and for weak microwave inputs, the relation between the S_{21} and g_0 is given by

$$S_{21} = \frac{8g_0^2\gamma_e\kappa_e^2 R_{\mathrm{PD}}^2 I_{\mathrm{rec}}^2}{\hbar\gamma^2\Omega_m^3\kappa^2 R_{\mathrm{load}}}, \tag{2}$$

where κ (γ) and κ_e (γ_e) are the total loss and external coupling rate of the optical (acoustic) mode, respectively. Ω_m is the frequency of the acoustic mode, and $R_{\mathrm{load}} = 50\ \Omega$ is the impedance of the input microwave source. Equation (2) is derived from the equation of motion for the dynamics of the acousto-optic cavity (see Section 3 of Supplement 1). We estimate the acousto-optic single-photon coupling strength to be $g_0 \sim 1.1$ kHz between the 2.17 GHz acoustic mode and the fundamental TE optical mode, which is in good agreement with our theoretical predictions (see Table S1, Supplement 1).

Another important figure of merit is the photon number conversion efficiency η from the microwave frequency to the optical sideband frequency, and it describes the device performance at the single-photon level. From the derivation described in Section 3 of Supplement 1, the photon number conversion efficiency η is given by

$$\eta = C_0 \cdot n_{\mathrm{cav}} \cdot \frac{2\gamma_e}{\gamma} \cdot \frac{2\kappa_e}{\kappa}, \tag{3}$$

where $C_0 = 4g_0^2/(\gamma\kappa)$ is the single-photon cooperativity, $n_{\mathrm{cav}} = \kappa_e I_{\mathrm{opt}}/(\Omega_m^2\hbar\omega_0)$ is the intracavity optical photon number for the blue-detuned pump light, and $2\kappa_e/\kappa$ ($2\gamma_e/\gamma$) describes the external coupling efficiency of the optical (acoustic) mode. Based on the experimentally extracted rates (Table S2), our acousto-optic cavity features a single-photon cooperativity $C_0 = 4\times10^{-8}$ and a photon number conversion efficiency $\eta = 0.0017\%$ for an optical power of $I_{\mathrm{opt}} = 1$ mW. This efficiency could be further improved by acoustic and photonic engineering, as will be discussed later in Section 7.

As shown in Eq. (3), the photon number conversion efficiency depends on both optomechanical cooperativity (C_0) and the microwave-to-mechanical coupling strength (described by $2\gamma_e/\gamma$). Recent progress of LN OMCs [12] has demonstrated unitary optomechanical cooperativity, but their microwave-to-mechanical coupling strength is as low as 10^{-8}, which would limit the overall photon number conversion efficiency. Benefiting from our up to 50% microwave-to-acoustic coupling to the thin-film acousto-optic resonator, this photon number conversion efficiency could be greater than that of the OMCs, even though the acousto-optic coupling strength is weaker than that of the OMCs.

6. DEMONSTRATION OF A MICROWAVE-PHOTONIC LINK

A microwave-photonic link enables low-loss long-haul transport and flexible manipulation of microwave signals using optical devices by upconverting microwave frequencies to optical frequencies. To benchmark our acousto-optic racetrack device, we demonstrate a narrowband microwave-photonic link using our acousto-optic racetrack cavity, and a link gain of 0 dB is achieved without the need of an optical amplifier within the link (after the modulation of our acousto-optic device), which would significantly increase the noise of the link. The optical pump light is amplified to ~500 mW by an erbium-doped fiber amplifier and is blue-detuned by the acoustic resonant frequency Ω_m from the optical resonance [Fig. 5(a)]. We estimate that ~150 mW of optical power is coupled into the suspended LN waveguide, resulting in ~50 mW reaching the photodiode. Importantly, no damage to the waveguide is observed, indicating the ability of our suspended thin-film LN devices to handle large optical powers. A high-power photodiode, with responsivity R_{PD} of 0.55 A/W (corresponding to a quantum efficiency of 40%), is used to detect and downconvert the optical signal that we generate from our racetrack acousto-optic transducer back to the microwave domain. With these parameters, we measure an overall microwave link gain of 0 dB at 1.572 GHz [Fig. 5(b)] for a small microwave input signal at -20 dBm. By reducing the fiber-to-chip coupling loss to the previously demonstrated value of 1.7 dB/facet [42], a microwave link with a gain of 6.6 dB may be achieved in principle, with the possibility of a gain of at least 9 dB if tapered fibers are employed [43,44].

Next, we characterize the response at higher powers of microwave input. With increasing microwave powers at the acoustic resonant frequency $\Omega_m \sim 2$ GHz, optical sideband dips are observed in the transmission spectra [Fig. 5(c)] that agree with

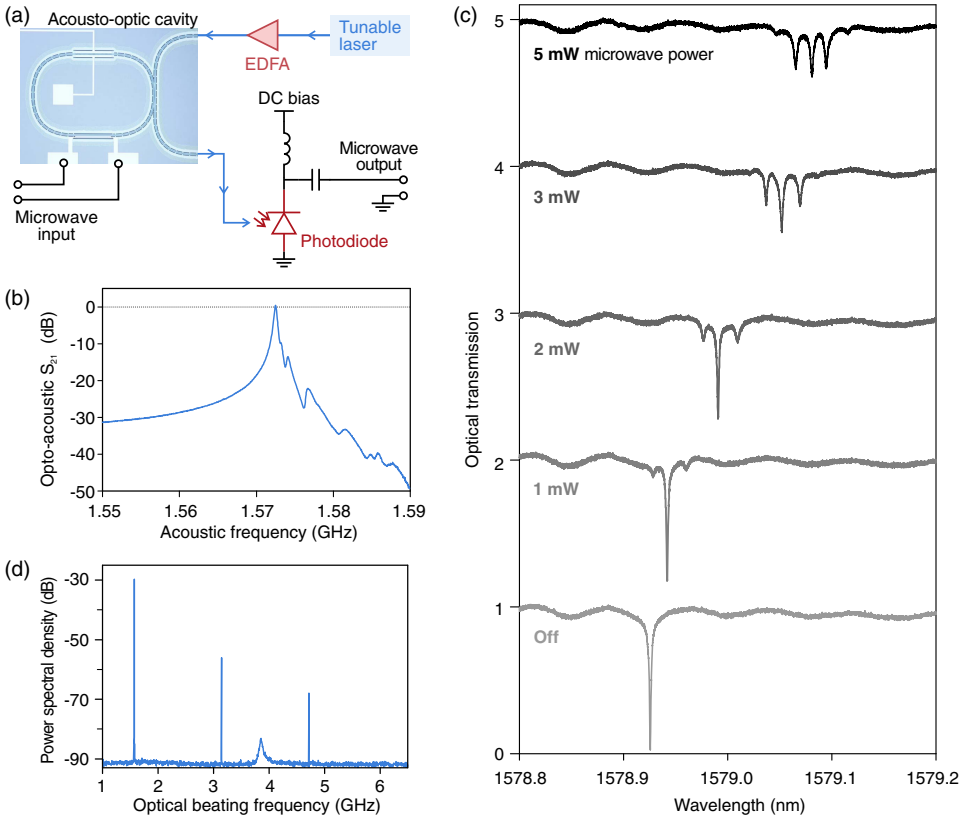

Fig. 5. Demonstration of a microwave-photonic link. (a) Experimental schematic. EDFA, erbium-doped fiber amplifier; (b) S_{21} spectrum features a peak microwave power transmission of ∼0 dB. The optical power received at the photodiode I_{rec} is 50 mW. (c) Optical transmission of the racetrack cavity for different microwave powers; (d) microwave spectrum of the photodiode output signal with a microwave power of 5 mW applied to the IDT of the thin-film acoustic resonator. The laser is blue-detuned from the optical mode by the acoustic resonant frequency Ω_m.

theoretical predictions (Fig. S3, Supplement 1). The redshift of the optical resonance with increasing input microwave powers results from the heating of the acoustic resonator. As a result of the efficient microwave-to-optical conversion, a pair of second-order sideband dips can be observed in the optical transmission spectrum with only 5 mW of microwave input power.

Parking the laser at Ω_m detuning from the optical mode, up to third-order harmonic signals are observed at the photodiode output with a microwave power of 5 mW [Fig. 5(d)]. The additional broad peak observed at 3.85 GHz is a result of the suspended optical racetrack cavity, since it is only observed when the pump laser is close to the optical resonance. We speculate that the acoustic mode along the suspended optical waveguide causes this additional peak by spontaneous Brillouin scattering, as our suspended racetrack cavity has a similar geometry with that in Ref. [45].

7. CONCLUSIONS AND OUTLOOK

We demonstrate an integrated acousto-optic platform on thin-film LN, which converts acoustic waves in the microwave domain to optical light by a generalized acousto-optic interaction. The efficient microwave-to-acoustic coupling has been achieved using our IDT-coupled LN thin-film acoustic resonator. This addresses the coupling issue of current OMC-based platforms using mechanically mediated microwave-to-optical converters. To further improve the photon number conversion efficiency, a variety of efforts in acoustic and photonic engineering can be made. For example, the acoustic resonator can be operated under vacuum and cryogenic environments to achieve higher Q factors, and the clamping loss of the suspended structures can be further reduced using phononic crystals [20]. Optical cavities defined by photonic crystal mirrors could improve the acousto-optic coupling strength g_0 with larger overlap with the acoustic resonator, while the presented racetrack cavity only partially sits in the acoustic resonator. Another order-of-magnitude improvement could be obtained by bringing both the pump light and generated optical sideband into resonance [3]. With a double optical resonance, which can be found in coupled cavities or due to scattering in a single ring cavity, the term Ω^2 (∼ GHz) in the denominator of intracavity optical photon number n_{cav} [Eq. (3)] is replaced by the optical cavity loss κ^2 (∼10 s of MHz) and could result in an improvement of 4 orders of magnitude.

Beyond microwave-to-optical conversion, our acousto-optic platform could also find applications in gigahertz frequency optical comb generation [46,47], on-chip optical routing, and optical mode conversion. In these applications, the acoustic resonator could strongly enhance the signal in the microwave domain and allow low microwave power operations. Compared to microwave electromagnetic resonators, the high acoustic fQ product and smaller acoustic mode volume of our on-chip acousto-optic resonator could enable quantum optomechanics at room temperatures with smaller footprints.

Funding. National Science Foundation (DMR-1707372, DMR-1231319, ECCS-1740296, ECCS-1810233); Office of

Naval Research (N00014-15-1-2761); Natural Sciences and Engineering Research Council of Canada; U.S. Department of Energy (DE-SC0019219).

Acknowledgment. N. S. acknowledges support by the Natural Sciences and Engineering Research Council of Canada (NSERC), the AQT Intelligent Quantum Networks and Technologies (INQNET) research program, and by the DOE/HEP QuantISED program grant, QCCFP (Quantum Communication Channels for Fundamental Physics).

See Supplement 1 for supporting content.

REFERENCES

1. D. Marpaung, J. Yao, and J. Capmany, "Integrated microwave photonics," Nat. Photonics **13**, 80–90 (2019).
2. G. Wendin, "Quantum information processing with superconducting circuits: a review," Rep. Prog. Phys. **80**, 106001 (2017).
3. A. Rueda, F. Sedlmeir, M. C. Collodo, U. Vogl, B. Stiller, G. Schunk, D. V. Strekalov, C. Marquardt, J. M. Fink, O. Painter, G. Leuchs, and H. G. L. Schwefel, "Efficient microwave to optical photon conversion: an electro-optical realization," Optica **3**, 597–604 (2016).
4. K. Stannigel, P. Rabl, A. S. Sørensen, P. Zoller, and M. D. Lukin, "Optomechanical transducers for long-distance quantum communication," Phys. Rev. Lett. **105**, 220501 (2010).
5. M. Tsang, "Cavity quantum electro-optics," Phys. Rev. A **81**, 063837 (2010).
6. M. J. A. Schuetz, E. M. Kessler, G. Giedke, L. M. K. Vandersypen, M. D. Lukin, and J. I. Cirac, "Universal quantum transducers based on surface acoustic waves," Phys. Rev. X **5**, 031031 (2015).
7. L. Fan, C.-L. Zou, N. Zhu, and H. X. Tang, "Spectrotemporal shaping of itinerant photons via distributed nanomechanics," Nat. Photonics **13**, 323–327 (2019).
8. A. P. Higginbotham, P. S. Burns, M. D. Urmey, R. W. Peterson, N. S. Kampel, B. M. Brubaker, G. Smith, K. W. Lehnert, and C. A. Regal, "Harnessing electro-optic correlations in an efficient mechanical converter," Nat. Phys. **14**, 1038–1042 (2018).
9. R. W. Andrews, R. W. Peterson, T. P. Purdy, K. Cicak, R. W. Simmonds, C. A. Regal, and K. W. Lehnert, "Bidirectional and efficient conversion between microwave and optical light," Nat. Phys. **10**, 321–326 (2014).
10. T. Bagci, A. Simonsen, S. Schmid, L. G. Villanueva, E. Zeuthen, J. Appel, J. M. Taylor, A. Sorensen, K. Usami, A. Schliesser, and E. S. Polzik, "Optical detection of radio waves through a nanomechanical transducer," Nature **507**, 81–85 (2014).
11. M. Forsch, R. Stockill, A. Wallucks, I. Marinkovic, C. Gärtner, R. A. Norte, F. van Otten, A. Fiore, K. Srinivasan, and S. Gröblacher, "Microwave-to-optics conversion using a mechanical oscillator in its quantum ground state," arXiv:1812.07588 (2018).
12. W. Jiang, R. N. Patel, F. M. Mayor, T. P. McKenna, P. Arrangoiz-Arriola, C. J. Sarabalis, J. D. Witmer, R. V. Laer, and A. H. Safavi-Naeini, "Lithium niobate piezo-optomechanical crystals," Optica **6**, 845–853 (2019).
13. K. C. Balram, M. I. Davanco, J. D. Song, and K. Srinivasan, "Coherent coupling between radio frequency, optical, and acoustic waves in piezo-optomechanical circuits," Nat. Photonics **10**, 346–352 (2016).
14. A. Vainsencher, K. J. Satzinger, G. A. Peairs, and A. N. Cleland, "Bi-directional conversion between microwave and optical frequencies in a piezoelectric optomechanical device," Appl. Phys. Lett. **109**, 033107 (2016).
15. J. Bochmann, A. Vainsencher, D. D. Awschalom, and A. N. Cleland, "Nanomechanical coupling between microwave and optical photons," Nat. Phys. **9**, 712–716 (2013).
16. L. Fan, X. Sun, C. Xiong, C. Schuck, and H. X. Tang, "Aluminum nitride piezo-acousto-photonic crystal nanocavity with high quality factors," Appl. Phys. Lett. **102**, 153507 (2013).
17. G. S. MacCabe, H. Ren, J. Luo, J. D. Cohen, H. Zhou, A. Sipahigil, M. Mirhosseini, and O. Painter, "Phononic bandgap nano-acoustic cavity with ultralong phonon lifetime," arXiv:1901.04129 (2019).
18. H. Liang, R. Luo, Y. He, H. Jiang, and Q. Lin, "High-quality lithium niobate photonic crystal nanocavities," Optica **4**, 1251–1258 (2017).
19. K. C. Balram, M. Davanco, J. Y. Lim, J. D. Song, and K. Srinivasan, "Moving boundary and photoelastic coupling in GaAs optomechanical resonators," Optica **1**, 414–420 (2014).
20. K. Fang, M. H. Matheny, X. Luan, and O. Painter, "Optical transduction and routing of microwave phonons in cavity-optomechanical circuits," Nat. Photonics **10**, 489–496 (2016).
21. M. J. Burek, J. D. Cohen, S. M. Meenehan, N. El-Sawah, C. Chia, T. Ruelle, S. Meesala, J. Rochman, H. A. Atikian, M. Markham, D. J. Twitchen, M. D. Lukin, O. Painter, and M. Lončar, "Diamond optomechanical crystals," Optica **3**, 1404–1411 (2016).
22. M. Eichenfield, J. Chan, R. M. Camacho, K. J. Vahala, and O. Painter, "Optomechanical crystals," Nature **462**, 78–82 (2009).
23. M. Lejman, G. Vaudel, I. C. Infante, I. Chaban, T. Pezeril, M. Edely, G. F. Nataf, M. Guennou, J. Kreisel, V. E. Gusev, B. Dkhil, and P. Ruello, "Ultrafast acousto-optic mode conversion in optically birefringent ferroelectrics," Nat. Commun. **7**, 12345 (2016).
24. A. S. Andrushchak, B. G. Mytsyk, H. P. Laba, O. V. Yurkevych, I. M. Solskii, A. V. Kityk, and B. Sahraoui, "Complete sets of elastic constants and photoelastic coefficients of pure and MgO-doped lithium niobate crystals at room temperature," J. Appl. Phys. **106**, 073510 (2009).
25. R. S. Weis and T. K. Gaylord, "Lithium niobate: summary of physical properties and crystal structure," Appl. Phys. A **37**, 191–203 (1985).
26. C. Wang, M. Zhang, X. Chen, M. Bertrand, A. Shams-Ansari, S. Chandrasekhar, P. Winzer, and M. Lončar, "Integrated lithium niobate electro-optic modulators operating at CMOS-compatible voltages," Nature **562**, 101–104 (2018).
27. C. Campbell, *Surface Acoustic Wave Devices and Their Signal Processing Applications* (Academic, 1989).
28. C. S. Tsai, "Wideband acousto-optic Bragg diffraction in $LiNbO_3$ waveguide and applications," in *Guided-Wave Acousto-Optics: Interactions, Devices, and Applications* (Springer, 1990), pp. 117–203.
29. H. Li, Q. Liu, and M. Li, "Electromechanical Brillouin scattering in integrated planar photonics," APL Photon. **4**, 080802 (2019).
30. Q. Liu, H. Li, and M. Li, "Electromechanical Brillouin scattering in integrated optomechanical waveguides," Optica **6**, 778–785 (2019).
31. S. A. Tadesse and M. Li, "Sub-optical wavelength acoustic wave modulation of integrated photonic resonators at microwave frequencies," Nat. Commun. **5**, 5402 (2014).
32. S. Kapfinger, T. Reichert, S. Lichtmannecker, K. Muller, J. J. Finley, A. Wixforth, M. Kaniber, and H. J. Krenner, "Dynamic acousto-optic control of a strongly coupled photonic molecule," Nat. Commun. **6**, 8540 (2015).
33. D. B. Sohn, S. Kim, and G. Bahl, "Time-reversal symmetry breaking with acoustic pumping of nanophotonic circuits," Nat. Photonics **12**, 91–97 (2018).
34. L. Shao, S. Maity, L. Zheng, L. Wu, A. Shams-Ansari, Y.-I. Sohn, E. Puma, M. N. Gadalla, M. Zhang, C. Wang, E. Hu, K. Lai, and M. Lončar, "Phononic band structure engineering for high-Q gigahertz surface acoustic wave resonators on lithium niobate," Phys. Rev. Appl. **12**, 014022 (2019).
35. Y. Yang, R. Lu, T. Manzaneque, and S. Gong, "1.7 GHz Y-cut lithium niobate MEMS resonators with FoM of 336 and fQ of $9.15x10^{12}$," in *IEEE/MTT-S International Microwave Symposium - IMS* (2018), pp. 563–566.
36. M. Zhang, C. Wang, R. Cheng, A. Shams-Ansari, and M. Lončar, "Monolithic ultra-high-Q lithium niobate microring resonator," Optica **4**, 1536–1537 (2017).
37. B. Desiatov, A. Shams-Ansari, M. Zhang, C. Wang, and M. Lončar, "Ultra-low-loss integrated visible photonics using thin-film lithium niobate," Optica **6**, 380–384 (2019).
38. M. Cherchi, S. Ylinen, M. Harjanne, M. Kapulainen, and T. Aalto, "Dramatic size reduction of waveguide bends on a micron-scale silicon photonic platform," Opt. Express **21**, 17814–17823 (2013).
39. L. Marculescu and G. Hauret, "Étude de l'effet Brillouin à température ordinaire dans le niobate de lithium," Compt. Rend. Acad. Sci. (B) **276**, 555–558 (1973).
40. L. Zheng, H. Dong, X. Wu, Y.-L. Huang, W. Wang, W. Wu, Z. Wang, and K. Lai, "Interferometric imaging of nonlocal electromechanical power transduction in ferroelectric domains," Proc. Natl. Acad. Sci. **115**, 5338–5342 (2018).
41. L. Zheng, D. Wu, X. Wu, and K. Lai, "Visualization of surface-acoustic-wave potential by transmission-mode microwave impedance microscopy," Phys. Rev. Appl. **9**, 061002 (2018).

42. L. He, M. Zhang, A. Shams-Ansari, R. Zhu, C. Wang, and L. Marko, "Low-loss fiber-to-chip interface for lithium niobate photonic integrated circuits," Opt. Lett. **44**, 2314–2317 (2019).
43. M. J. Burek, C. Meuwly, R. E. Evans, M. K. Bhaskar, A. Sipahigil, S. Meesala, B. Machielse, D. D. Sukachev, C. T. Nguyen, J. L. Pacheco, E. Bielejec, M. D. Lukin, and M. Lončar, "Fiber-coupled diamond quantum nanophotonic interface," Phys. Rev. Appl. **8**, 024026 (2017).
44. A. Sipahigil, R. Evans, D. Sukachev, M. Burek, J. Borregaard, M. Bhaskar, C. Nguyen, J. Pacheco, H. Atikian, and C. Meuwly, "An integrated diamond nanophotonics platform for quantum-optical networks," Science **354**, 847–850 (2016).
45. N. T. Otterstrom, R. O. Behunin, E. A. Kittlaus, Z. Wang, and P. T. Rakich, "A silicon Brillouin laser," Science **360**, 1113–1116 (2018).
46. A. Rueda, F. Sedlmeir, M. Kumari, G. Leuchs, and H. G. L. Schwefel, "Resonant electro-optic frequency comb," Nature **568**, 378–381 (2019).
47. M. Zhang, B. Buscaino, C. Wang, A. Shams-Ansari, C. Reimer, R. Zhu, J. M. Kahn, and M. Lončar, "Broadband electro-optic frequency comb generation in a lithium niobate microring resonator," Nature **568**, 373–377 (2019).